RESEARCH ARTICLE

ADVANCED
INTELLIGENT
SYSTEMS
Open Access

www.advintellsyst.com

Ultralight Smart Patch with Reduced Sensing Array Based on Reduced Graphene Oxide for Hand Gesture Recognition

Yuchi Liu, Xiangpeng Liang, Haonan Li, Haitao Deng, Xinran Zhang, Danliang Wen, Mengyao Yuan, Hadi Heidari, Rami Ghannam,* and Xiaosheng Zhang*

Flexible sensors for hand gesture recognition and human–machine interface (HMI) applications have witnessed tremendous advancements during the last decades. Current state-of-the-art sensors placed on fingers or embedded into gloves are incapable of fully capturing all hand gestures and are often uncomfortable for the wearer. Herein, a flake-sphere hybrid structure of reduced graphene oxide (rGO) doped with polystyrene (PS) spheres is fabricated to construct the highly sensitive, fast response, and flexible piezoresistive sensor array, which is ultralight in the weight of only 2.8 g and possesses the remarkable curved-surface conformability. The flexible wrist-worn device with a five-sensing array is used to measure pressure distribution around the wrist for accurate and comfortable hand gesture recognition. The intelligent wristband is able to classify 12 hand gestures with 96.33% accuracy for five participants using a machine learning algorithm. To showcase our wristband, a real-time system is developed to control a robotic hand via the classification results, which further demonstrates the potential of this work for HMI applications.

1. Introduction

Hand gesture is an important nonverbal communication for conveying information through visual perception. With the burgeoning demand for interfaces that enable humans to seamlessly interact with machines, gesture recognition systems have been fast developed using vision and wearable-based technologies.

Y. Liu, H. Li, H. Deng, X. Zhang, D. Wen, X. Zhang
School of Electronic Science and Engineering
University of Electronic Science and Technology of China
Chengdu 611731, China
E-mail: zhangxs@uestc.edu.cn

Y. Liu, X. Liang, M. Yuan, H. Heidari, R. Ghannam
James Watts School of Engineering
University of Glasgow
Glasgow G12 8QQ, UK
E-mail: rami.ghannam@glasgow.ac.uk

In fact, wearable electronics hold great promise in healthcare monitoring,[1–4] virtual reality,[5,6] and robot control,[7,8] which benefit from attractive features such as lightweight, low cost, flexibility, and adaptability to different environments.

In recent years, different types of wearable sensors have been developed for hand gesture recognition, including the strain sensor,[9,10] piezoelectric sensor,[11,12] triboelectric sensor,[5,13–15] etc. In the literature, these sensors are either placed directly on the finger or integrated into a glove, enabling finger movements to be captured more accurately.[9,10,13,16,17] For instance, flexible cowpea-structured piezoelectric sensors are placed on the fingers to monitor the motion of the human hand, thus enabling remote control of the robotic palm.[18] Besides, gesture recognition systems based on electromyography (EMG) place high-density electrodes on the forearm to monitor arm muscle activity while performing gestures.[19–21] However, these methods require many attachments on the hand or forearm, which are cumbersome and uncomfortable, hindering the convenience of practical use. The wrist, in this case, has attracted tremendous interest in gesture recognition due to its large number of tendons and muscles, which provides comprehensive information on hand movements.

In this regard, wrist-worn devices are more natural and comfortable in recognizing hand gestures.[22] For example, a wristband device was integrated with surface electromyography (sEMG) and inertial measurement unit (IMU) sensors to detect air and surface gestures, where the sensors were encapsulated in 3D printed boxes.[23] In addition, another smart wristband was proposed using hybrid generators consisting of the triboelectric sensor and piezoelectric sensor to recognize 26 letters.[24] However, these structures of the sensor or wristband device are rigid and significant in size, which is uncomfortable to wear and hard to detect slight muscle contraction and expansion, which would affect the accuracy of the recognition results. Therefore, this article presents a fully flexible and lightweight smart wristband based on the piezoresistive sensor for hand gesture recognition. The weight of the wristband is only 2.8 g which can fit well on the human wrist without interfering with daily work.

Piezoresistive sensors, whose resistance can be tuned by the mechanical forces imposed on the surfaces, have been widely

investigated and used in gesture recognition due to their excellent sensitivity and continuous detection capabilities.[22] Various piezoresistive materials and structures have been investigated to realize the transduction. It was previously demonstrated that the nano/microgeometrical structures yield a greater sensitivity.[25–28] For example, the hierarchically microstructure-bioinspired flexible piezoresistive sensor with microdome structure exhibits an ultrahigh sensitivity of 53 kPa^{-1}.[29] However, these microstructures are expensive and require complex fabrication procedures. In contrast, the low cost and less complex fabrication processes involving reduced graphene oxide (rGO), which has a 2D nanosheet layer structure, exhibit high conductivity and robust mechanical strength, making it a promising candidate for flexible piezoresistive sensors.[30–34] This article proposes a piezoresistive sensor based on a flake-sphere composite configuration in which rGO fragments are doped with polystyrene (PS) spheres to achieve both high sensitivity and flexibility. The resistance change under pressure was related to the size and weight ratio of the doping PS sphere. Our flexible rGO/PS sensors achieved 66% resistance change when doped with 2 μm PS spheres. The rGO-based sensor also promises high mechanical durability (1000 times) and fast response time (186 ms), which offers excellent potential in wearable devices and micro-electromechanical systems (MEMS) devices.

In this article, we present a wearable hand gesture recognition system based on two parts: a flexible piezoresistive wristband that measures the pressure distribution around the wrist, and an interface for intelligent gesture classification. Our rGO-based flexible piezoresistive sensors were doped with PS spheres to achieve high sensitivity. These sensors demonstrate good mechanical durability, high sensitivity, excellent flexibility, and quick response time. Our high-performance wristband consisted of an array of five rGO/PS sensors for detecting subtle wrist movement information. In the meantime, the developed system was successfully demonstrated to realize the recognition of 12 different hand gestures with an accuracy of 96.33% with the help of a machine learning algorithm. Furthermore, a human–machine interface (HMI) application was also designed to showcase that our system can wirelessly control a robotic hand.

2. Sensor Fabrication and Optimization

2.1. Sensor Fabrication

The fabrication procedure of the rGO/PS piezoresistive sensor is schematically shown in **Figure 1**. First, the polydimethylsiloxane (PDMS) substrate was prepared. The PDMS monomer and curing agent (Sylgard 184) were mixed for 15 min with a weight ratio of 10:1 and then degassed in a vacuum chamber for 30 min. The bubble-free PDMS slurry was poured into the prepared mold and cured at 70 °C for an hour. The as-prepared PDMS film was treated with air plasma for 30 s to remove the dust and improve the surface adhesion.

The next step involved preparing the flexible AgNW electrodes, as shown in Figure 1a. The AgNW solution (Nanjing XFNANO Materials Tech Co., Ltd.; diameter: 50 nm, length: 20–60 μm) was first diluted to 2.0 mg mL^{-1} with ethyl alcohol by 300 r min^{-1} magnetic stirring for 30 min. The AgNW solution was sprayed on the PDMS substrate every 30 s through a 3D printed mask for a total of 20 times. Afterward, the AgNW/PDMS film was thermally annealed in the oven at 150 °C for 30 min to allow junctions to form between AgNWs, thereby increasing the electrical conductivity.
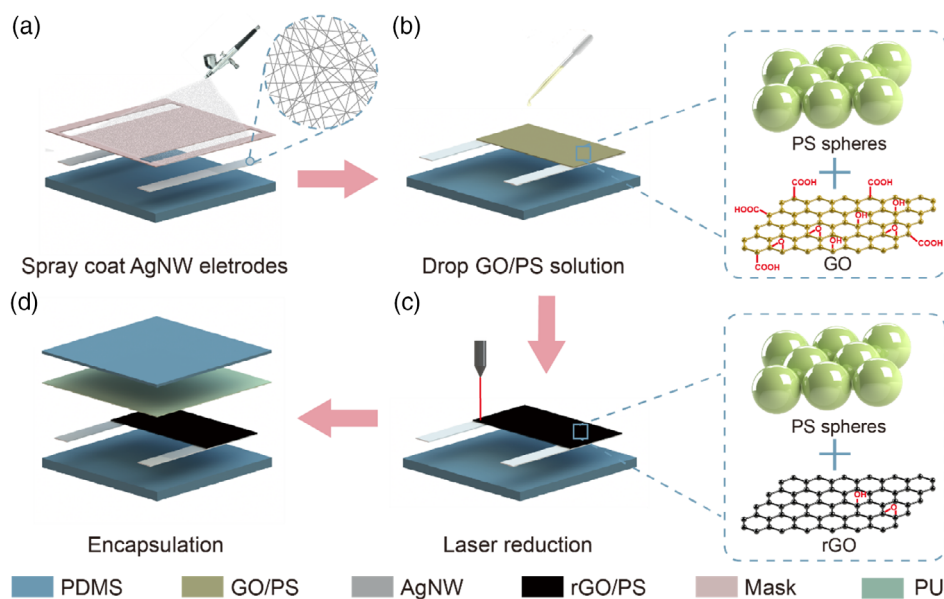

Figure 1. Schematic illustration of the fabrication process of the flexible rGO/PS piezoresistive sensor. a) 2 mg mL^{-1} AgNW ethanol-based solution was spray coated on the as-prepared PDMS film. b) Doped the mixed GO/PS solution on the AgNW electrodes and the PDMS film, and heat for 3 h until it obtained the dry film. c) The GO/PS film was patterned by laser-induced reduction that directly converted GO into rGO, where most of the oxygen functional groups were removed. The color of the functional layer changed from dark brown to black. d) Finally, the sensor was encapsulated by a thin PU film and a PDMS layer.

The functional layer of the piezoresistive sensor consisted of rGO fragments and PS spheres. The $2.0 \, mg \, mL^{-1}$ GO solution was prepared by adding 16.0 mg GO powder (Suzhou Tanfeng Graphene Technology Co., Ltd.; lamella diameter: 0.2–10 μm, purity: 96%) into 8.0 mL of deionized water. The solution was exposed to a 50 W ultrasonic transducer (bisafer250up, 19–25 kHz) for 15 min. Then PS spheres (Tianjin BaseLine ChromTech Research Centre; 2.5% w/v) were added into the GO solution, followed by leaving the mixture in an ultrasonic bath for another 15 min. Next, the 300 μL mixed solution was dropped on PDMS and AgNW in an area of $15 \times 8 \, mm^2$. The sample was placed in the oven at 50 °C for 3 h to get a thin GO/PS film (Figure 1b). The film was patterned by a laser engraving machine (Ruijie RJ-4040) which directly converted the GO film to rGO by Joule heat (Figure 1c). Finally, a polyurethane (PU) film was placed on the surface of the rGO/PS layer to isolate the uncured PDMS from destroying the rGO interlayer structure, and also fix the wire on the AgNW electrodes. In the end, the whole sensor was encapsulated by PDMS (Figure 1d).

2.2. Tests and Measurement

The surface morphology of the sensing film was characterized by field emission scanning electron microscopy (SEM) (S-4800 FESEM, Hitachi and JSM-6490LV, JEOL Ltd.), transmission electron microscope (TEM) (FEI Tecnai G2 F20 S-TWIN), and atomic force microscope (AFM) (Digital Instruments Dimensions 3100). The Raman spectra of the film were obtained using a HORIBA iHR 550 with 532 nm laser excitation. Compression properties were tested under a push and pull tester (HLB, HANPI), and the electrical properties were measured using an LCR meter (KEYSIGHT E4980AL) at room temperature. A vibration platform consisting of a signal generating system (33250A, Agilent), a power amplifier (YE5872A, Sinocera Piezotronics, Inc.), and a shaker (YE5872A, Sinocera Piezotronics, Inc.) was used to measure the durability of the rGO/PS sensor in thousands of work cycles.

2.3. Sensor Optimization

The photograph of the fabricated rGO/PS sensor is shown in **Figure 2**i. The piezoresistive sensor was constructed with a PDMS substrate, AgNW electrodes, and a functional film with deposited rGO and PS spheres mixing solutions. The sensor was encapsulated by a thin PU film to maintain the integrity of the functional layer structure and a PDMS layer to prolong the durability of the sensor. The fabricated sensor exhibits excellent flexibility and can be folded 180° without damaging
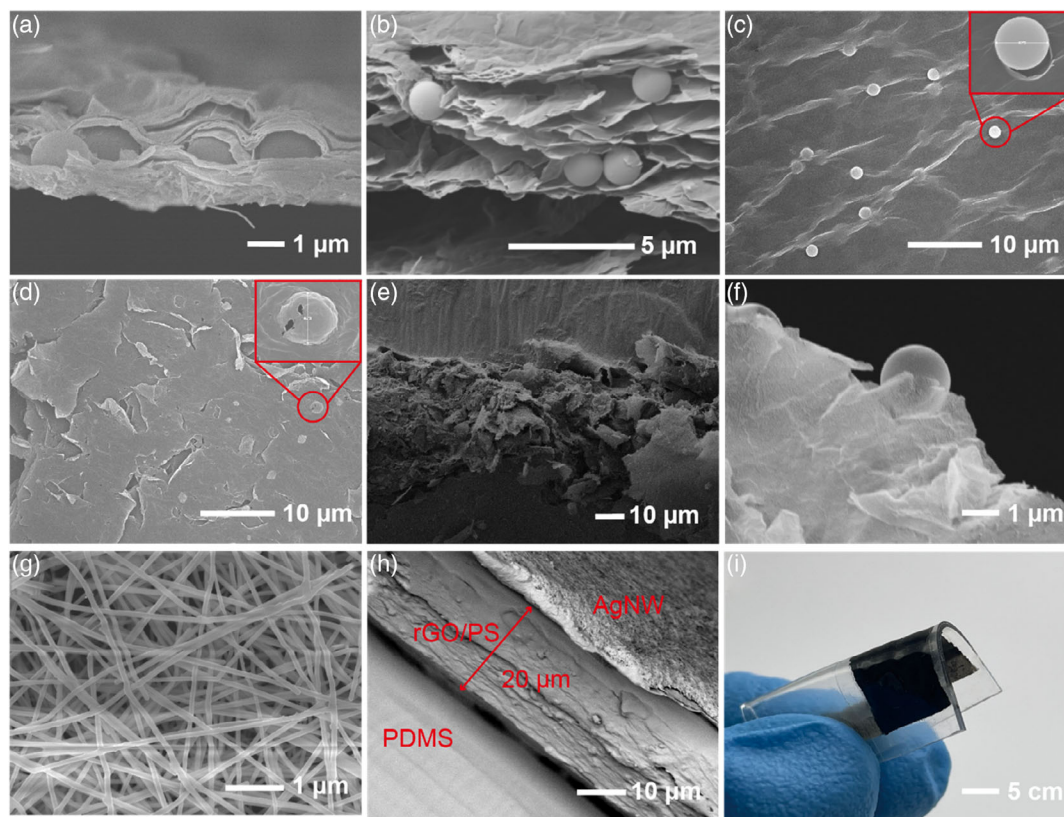

Figure 2. a) Cross-sectional SEM image of the fabricated GO/PS sensor. b) Cross-sectional SEM image of the fabricated rGO/PS sensor. c) Surface SEM image of GO/PS structure. d) Surface SEM image of rGO/PS structure. e) Cross-sectional SEM image of fracture surface of the rGO/PS sensor. f) A magnified SEM image of the fracture surface, showing that the PS spheres are sandwiched between the rGO layers. g) Surface SEM images of AgNW electrodes. h) Cross-sectional SEM image of sensor structure, where the thickness of the functional layer is around 20 μm. i) Photograph of the fabricated rGO/PS sensor with the dimension of $20 \times 20 \times 0.5$ mm, which shows outstanding flexibility of the developed sensor.

**ADVANCED
SCIENCE NEWS**

www.advancedsciencenews.com

**ADVANCED
INTELLIGENT
SYSTEMS**

www.advintellsyst.com

the performance of the device, which further shows the excellent feasibility of the sensors for wearable applications. The surface morphology of the AgNW electrodes are shown in Figure 2g, indicating the formation of a conductive surface, where the sheet resistance of the AgNW was $3.2 \, \Omega \, cm^{-1}$. The detailed morphologies of single AgNW were undertaken by TEM and AFM, shown in Figure S1c,f, Supporting Information, where the diameter of AgNW is around 50 nm. The excellent electrical conductivity and flexibility make AgNW a good material for flexible electrodes in this sensor. The thickness of the whole device is around 500 μm, and the functional layer is about 20 μm (Figure 2h).

In this article, the GO film was treated using a CO_2 laser through a programmable patterning manner. In comparison with other reduction techniques such as chemical reduction or oven treatment, laser scribing is a convenient and fast way to formulate rGO and allows patterning of the conducting channels.[33] By laser scribing, GO was reduced to rGO according to the photothermal effect. With the increasing local temperature in the patterned laser location, water was evaporated and oxygen-containing groups (OCG) were removed from the GO film,[35] as illustrated in Figure S2a, Supporting Information. The rapid release of OCG made rGO form a highly porous structure. The cross-sectional SEM images of GO film (Figure 2a) and rGO film (Figure 2b) demonstrate that laser reduction has successfully reduced GO into rGO and confirm that the rGO surface is composed of stacked layers. The fractured surface of the developed sensor was also observed by using SEM. From Figure 2e, rGO shows a crumpled and overlapped multilayer structure. In the high magnified figure (Figure 2f), we can see the PS spheres were sandwiched between the rGO layers, enhancing the gap between the stack layers, which led to the increasing contact resistance of the developed sensor.

The surface morphologies of GO and rGO are shown in Figure 2c,d, indicating that the surface of rGO becomes much rougher compared to that of GO. Furthermore, the morphologies of GO and rGO were characterized in detail by AFM and TEM because they are tools that are frequently applied to nanosize materials. Figure S1a, Supporting Information presents the surface morphology of GO that is flat and smooth, while it appears wrinkled after laser reduction (Figure S1b, Supporting Information). AFM images of GO and rGO are shown in Figure S1e,f, Supporting Information. The height of the rGO sheets is around 6.18 nm, thinner than the GO sheets (6.77 nm). Compared with the previous report,[36] the tested samples are multilayer. In this case, the reduction in the thickness of rGO could be due to the removal of OCG. It is worth noting that after laser reduction, the color of the patterned area would change from dark brown to black (Figure S3e, Supporting Information).

To further prove the reduction of the GO film, Raman spectroscopy was conducted to characterize the surface of the sensing film. Raman spectroscopy is a widely used technique for studying structural information of carbon-based materials. The main features in the Raman spectra of graphitic carbon-based materials are the G and D peaks, where the D band is applied to characterize structural defects, amorphous carbon, or edges that split the symmetry and selection rule,[37,38] and G-band is associated with graphitic carbon.[35] The D/G intensity ratio (I_D/I_G) ratio is an index of the disorder in graphene. From Figure S2b,

Supporting Information, the decreasing I_D/I_G from 0.80 to 0.78 demonstrates the removal of the oxygen functional groups and the restoration of sp^2 domain, so that most GO have converted to the rGO through the laser reduction process.

The resistance of the rGO sensor is mainly attributed to two parts: the intrinsic resistance (R_i) of rGO fragments and the contact resistance (R_c) of stacked rGO layers, as shown in **Figure 3**a. The total resistance is given by $R_{Total} = R_i + \Delta R_c$. When the sensor is under pressure, the distance between two neighboring interlayers in the rGO will decrease, resulting in a decrease in the internal resistance R_c and an increase in conductivity. As a result, the total resistance of the sensor will decrease. For nondoped rGO, the fragments are stacked closely due to deposition and thermal expansion, which leads to small contact resistance. To improve the sensitivity of the sensor, the PS spheres were doped as insulators to change the stacking pattern of the rGO fragments. The PS spheres were embedded between rGO fragments layers, enhancing the gap between the stack layers, which led to the increasing contact resistance of the film. The between-layer fragment conduction channel is the dominant working principle in this case. Under pressure, the spaces between the rGO fragments become narrow, which results in the formation of multiple conductive channels. The conducting network makes the resistance of the rGO/PS sensor sensitive to pressure.

To investigate the role of the PS spheres, a series of experiments were conducted to study the pressure behavior of the sensors by adjusting the doping size and doping ratio of PS spheres. The sensing performance of the device was tested under an external mechanical force from 0 to 10 N. First, different PS spheres diameters varied from 80 nm to 2 μm were investigated. From Figure 3c, the maximum resistance change is over 47% with 2 μm doping PS spheres at 0.2 wt% doping ratio under 10 N, which is almost 3 times larger than the nondoped rGO sensor. At the small size of the doping spheres (80 nm), the maximum resistance decreases to 35%. When the large size spheres are placed between the rGO fragments, the more significant gap makes the between-layer conducting channels would partially disconnect, thereby introducing a high resistance value at the initial state. When applying external mechanical stresses on the sensor, the resistance of the sensor significantly decreases because the rGO fragments own closer contacts and more contacting sites. Therefore, the sensitivity of the device increases with larger size doping PS spheres.

To further study the effect of PS spheres on the sensor, the resistance changes of rGO film doped with 2 μm PS spheres of different weight ratios (0.1, 0.2, and 0.4 wt%) were also investigated. At a small doping ratio (0.1 wt%), the space between adjacent PS spheres was large, which makes it difficult for rGO fragments to separate. Thus, the remaining contacting points will influence the sensitivity of the device. A lower doping ratio results in small spacings between adjacent PS spheres, which leads to fewer device contacting points in the initial state. Sufficient space between fragments allows the device to create more contacting channels under external forces. As a result, the resistance change of the sensor increases as the weight ratio of PS spheres increases, as shown in Figure 3d. However, the proportion of PS spheres cannot consistently be increased. When the weight ratio of spheres is larger than 0.4 wt%, the
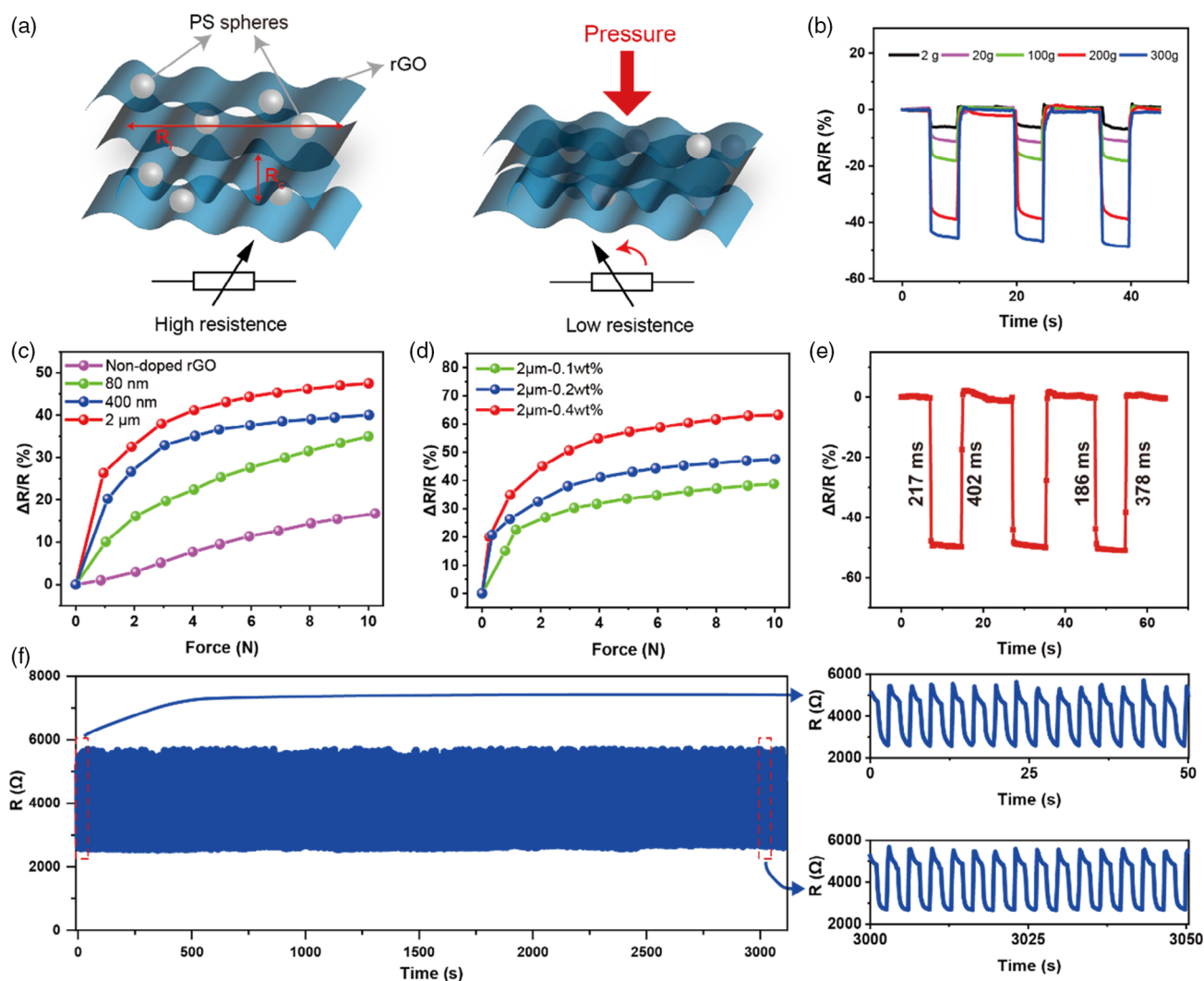
Figure 3. a) The sensing mechanism of the piezoresistive sensor. b) The resistance change of the rGO/PS sensor depends on different weights. c) The relationship between applied force and resistance changes with different doping PS spheres sizes. d) The relationship between applied force and resistance changes with different doping PS sphere weight ratios. e) The piezoresistive sensor shows rapid response and relaxation time. f) Test the repeatability performance of 1000 cycles under a pressure of 3 N.

surface of the rGO film arises some small cracks (Figure S3b,c, Supporting Information). Therefore, the 0.4 wt% doping PS sphere performs best as the resistance change reaches 66% under 10 N pressure.

Moreover, to estimate the detection limit, the resistance change of the rGO/PS device is measured as the load decreases. Figure 3b shows the pressure dependence of the resistance change ratio of the rGO/PS sensor, where the resistance changes about 6% under 2 g weight, which is a testament to the outstanding sensitivity of our piezoresistive sensor. Furthermore, the piezoresistive sensor shows rapid response and relaxation properties to instantaneous pressure with good reproducibility. The test was repeated 3 times, and the minimum response and relaxation times were about 186 and 378 ms, respectively (Figure 3e). In addition, the durability of the rGO/PS sensor was tested using a stable vibration platform. To evaluate the mechanical durability of the fabricated sensor, the

loading–unloading test was performed under 3 N force and 0.3 Hz frequency. After 1000 cycles, the total resistance and waveform were almost unchanged (Figure 3f).

As the developed flexible piezoresistive sensor can work as a wearable device, the stability of the sensor in different humid environments is necessary for practical applications. Herein, the resistance of the sensor under different humidity (from 40.46% to 93.2%) was tested. Although the relative humidity changed by over 40%, the resistance of the developed sensor remained stable (Figure S4a, Supporting Information). Besides, the responses of the sensor during finger tapping movements in air and water at room temperature were also evaluated. As shown in Figure S4b, Supporting Information, it is clearly seen that the resistance changes of the sensor in air and water were similar. All the above results show that the sensor exhibits good waterproof performance. Therefore, high sensitivity, fast response, excellent

stability, outstanding flexibility, and waterproofness give the sensor great advantages in wearable systems.

3. Hand Gesture Recognition

The superior performance results of our fabricated rGO/PS sensors enabled us to integrate them in a wristband device. Photographs of our wristband consisting of an array of five flexible rGO/PS piezoresistive sensors are shown in Figure S3g,h, Supporting Information. A machine learning algorithm was used to intelligently classify different hand gestures. Overall, our wearable system comprised a five-channel sensor wristband, a Bluetooth module, and a computer terminal.

The rGO/PS piezoresistive smart wristband converted pressure signals from tendon movements around the wrist to resistance variations that were then transferred to the voltage readings accordingly through the voltage divider circuit with an additional 5 kΩ resistor, according to the sensors' initial resistance. Afterward, the five-channel output voltage signals were transmitted wireless using an Arduino Nano Bluetooth module to a computer terminal. Data were collected using a LabVIEW interface with a sampling rate of 40 Hz and stored as a 5D vector in the computer for post processing.

The flexible wristband was placed on the left wrist of the subjects by the Velcro strap under comfortable tightness without blood restriction, pain, and movement limitation. Three sensors were placed on the underside of the wrist because of the high density of tendons in this location, while the other two sensors were fixed on the backside. For hand gesture recognition, five healthy subjects (three females and two males) aged between 23 and 27 were invited to take part in this experiment. The average wrist circumference of the five subjects was 161 ± 9 mm, and two of them were used to wearing a mechanical watch during their daily life. Before the experiment, all subjects were provided informed written consents and the experiments had been approved by the Ethics Committee of university.

All subjects were instructed in advance about the data collecting process and the way of wearing the wristband. The subjects sat in front of a desk and put their elbow on the desk with their forearm raised. The subjects were asked to perform 12 different hand gestures, including both finger flexion and wrist movements. Each subject conducted two trials on one gesture: one record contains ten repetitive gestures as a training set to train the classification model, and the other record contains five repetitions to test the accuracy of the classification algorithm in the recognition step. During the test, the subjects held each gesture for 2 s and rested for 5 s between gestures. The subjects rested for 2 min between each trial to avoid fatigue. The total experiment time for each subject was around 1 h.

Figure 4b presents the corresponding signals and their pressure maps on the wristband for 12 hand gestures. Figure 4b also shows the pressure level on each sensor and demonstrates the relationship between the gestures and their corresponding pressure values at the wristband locations. The acquired data are a mixture of output data from the rGO/PS sensors, time-varying offset, and noise. This noise was challenging to completely eliminate using the analogue conditioning circuit because it may come from sensors, equipment, power lines, or electrical radiation from the environment. A low pass filter was used to remove undesirable noise in this case. In the meantime, the baseline drift was also removed. The output signal of the piezoresistive sensor usually showed one noticeable mutation generated by the motion. Due to this characteristic, peak finding was used to detect mutations and their locations for the input vector. After finding peaks in the signal, 200 points were taken before and after the peak to get a complete dynamic gesture signal. To avoid intercepting the same data multiple times, the spacing between adjacent peaks should be more than 300 points. Herein, the whole signal was truncated to small segments according to the maxima of gesture signals.

The numerical data from the piezoresistive sensor varied significantly from one participant to another. Notably, the difference in wrist size, tendon strength, sensor location, and gesture habit for subjects would affect the overall dataset. In this case, instead of using raw data to feed the support vector machine (SVM) classifier, 35 statistical features were chosen as more compact and representative information to characterize the data, including mean, maximum, minimum, peak to peak, variance, percentiles, as well as the mean of the cross-correlation function contains the autocorrelation sequences for each channel of the dataset. The details of the feature extraction can be found in Table S1, Supporting Information.

A polynomial-kernel SVM was implemented to train the preprocessed features and reconstruct hand gestures. A kernel function of the 3-polynomial order was used to map the information to a higher dimension. The overall classification accuracy of the trained model for hand gesture recognition was 96.33%. The confusion matrix of the classification result is shown in Figure 4c. The matrix row represents the test samples in an actual class, while the column represents a predicted class. The frequent misclassification occurred between gesture 7 and gesture 12, where they have similar pressure patterns on the wristband.

For only the finger flexion, the accuracy reached 97%. Meanwhile, the accuracy of the wrist movements can achieve 100% because movements are more distinguishable. The confusion matrix is shown in Figure S5, Supporting Information. For visualization purposes, t-distributed stochastic neighbor embedding (t-SNE) was performed on the feature vectors. t-SNE is a popular nonlinear dimensionality reduction method that is well suited to visualizing high-dimensional datasets. Using data visualization methods, Figure 4d demonstrates the feature clustering result of 12 gestures for the input layer in a 2D space, where each color represents a single gesture group.

A detailed comparison of our system with existing state-of-the-art wristband devices is shown in **Table 1**. The selected publications are the state-of-the-art studies with the following criteria: 1) published in recent 5 years, 2) wrist-worn sensors for gesture recognition, 3) machine learning algorithms were used for classification, and 4) yielded acceptable results. Our custom-designed wristband is fully flexible and lightweight, which is essential for device wearability. In comparison with other wrist-worn methods, the rGO/PS flexible wristband demonstrated in this article has fewer sensor channels while achieving higher classification results.

A proof-of-concept real-time control for HMI was developed, allowing humans to interact with a mechanical hand by hand gestures using the SVM algorithm (Figure 4a). The rGO/PS
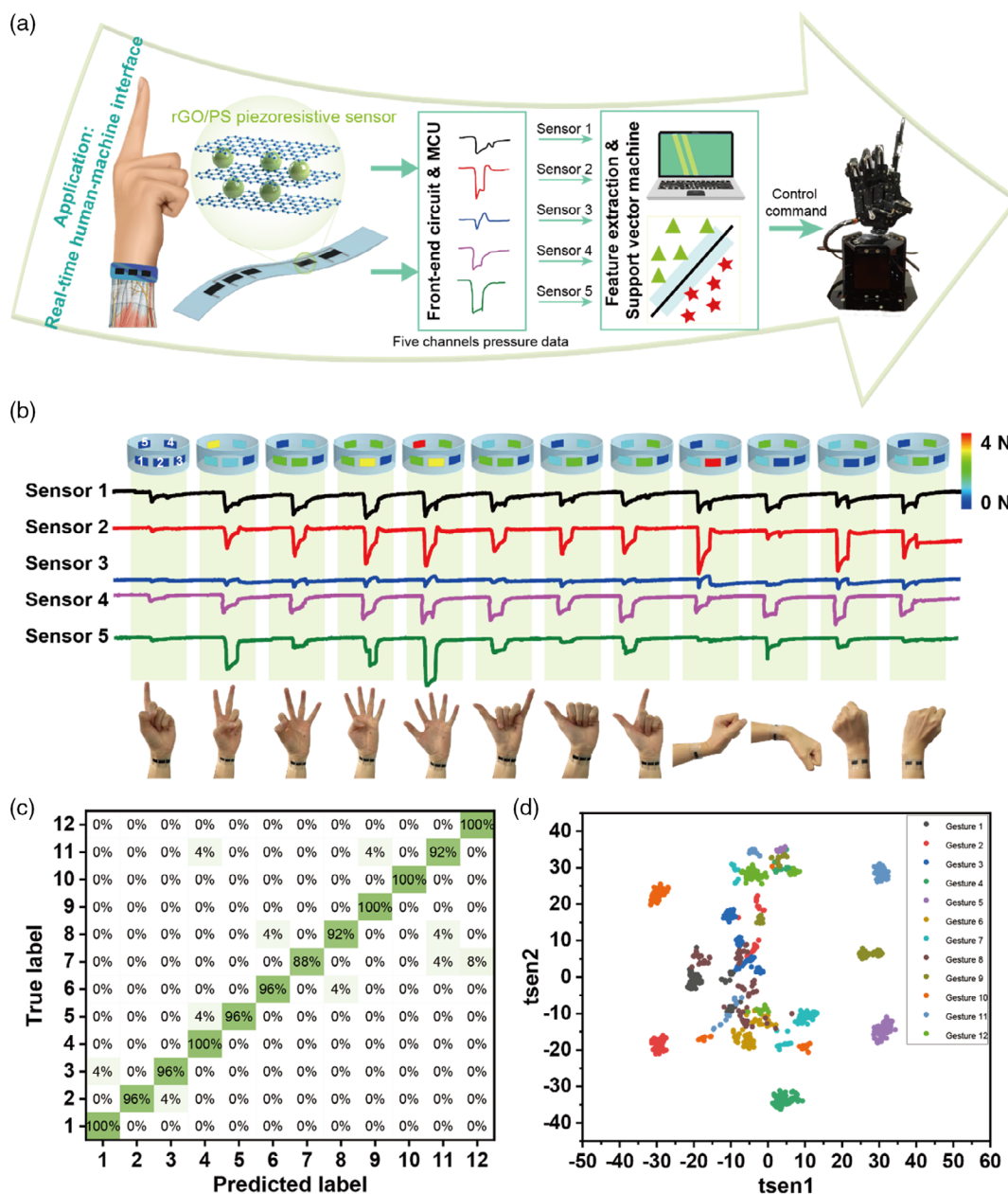
Figure 4. a) The schematic diagram of the proof-of-concept real-time control for HMI. b) Generated signal patterns for different hand gestures, and the corresponding pressure maps on the smart wristband. c) Classification confusion matrix for all 12 hand gestures; the accuracy is 96.33%. d) t-SNE visualization for all 12 gestures.

wristband was bound to the user's wrist to capture the tendon movements for different hand gestures. Moreover, signals generated by the piezoresistive sensors were transmitted wirelessly to the computer. After the preprocessing, each gesture signal was windowed to perform feature extraction. A LabVIEW interface displayed the real-time signals and the recognition results (Figure S6, Supporting Information). The results were transmitted to the robotic hand for real-time control. As shown in the Video S1, Supporting Information, different hand gestures were successfully translated from the human hand to the robotic hand. This real-time HMI application, which has been integrated with flexible

rGO/PS sensors, shows excellent capability in continuous human motion monitoring and robot control, which have a promising potential for the use in remote robot-assisted precision operations.

4. Conclusion

A flexible and highly sensitive piezoresistive sensor has been demonstrated, as well as its application in a wearable hand gesture recognition system. The sensor was deposited with a mixed solution of rGO and PS spheres, where the spheres acted as

Table 1. Performance comparison of hand gesture recognition system with rGO/PS flexible wristband and similar wristband products.

Sensor type	Number of sensors	Number of gestures	Number of participants	Algorithm	Accuracy	Flexible	Weight	Ref.
Triboelectric + piezoelectirc	8	26	Not mention	LDA	92.6%	No	Not mention	[24]
sEMG + IMU	4 sEMG + 1 IMU	8 air gesture + 4 surface gesture	4	LDA	92.8%/88.8%	No	56 g	[23]
Piezoelectric sensor	6	5	1	SVM	97%	No	1.8 g + 18.6 g	[12]
Barometric pressure sensor	10	19	10	LDA/SVM/KNN	94%	No	3.7 g + 18.6 g	[39]
Capacitive sensor	5	3	1	SVM and DAG	90%	No	Not mention	[40]
Electrical impedance tomography	16	8	2	ANN	99.5%	No	Not mention	[41]
Microphones	40	36	10	LDA/SVM	91%	No	Not mention	[42]
Inertial sensor	1	12	5	ADBA	99.2%	No	26 g	[43]
Piezoresistive sensor	5	12	5	SVM	96.33%	Yes	2.8 g	This work

insulators to separate the rGO fragments, resulting in a larger contact resistance change under pressure. We observed that doping different sizes and weight ratios of spheres influenced the sensing performance of the device. Therefore, by optimizing our design, a maximum resistance change of 66% was achieved when doping 2 μm spheres at 0.4 wt%, which is more than 4 times higher than nondoped rGO sensors.

Therefore, a highly flexible wristband was designed based on rGO/PS sensors to capture pressure distribution around the wrist. Data processing methods were used to truncate signal segments and extract feature information. In combination with an SVM classifier, 12 hand gestures were successfully recognized with a classification accuracy of 96.33%. To further support the use of our wristband device in an HMI application, we developed a real-time system that allows the user to control a robotic hand. The above results suggest that the flexible rGO/PS piezoresistive sensor offers excellent characteristics to assemble smart learning algorithms for next-generation wearable HMI.

Supporting Information

Supporting Information is available from the Wiley Online Library or from the author.

Conflict of Interest

The authors declare no conflict of interest.

Data Availability Statement

The data that support the findings of this study are available on request from the corresponding author. The data are not publicly available due to privacy or ethical restrictions.

[1] N. M. Mahmoud, H. Fouad, A. M. Soliman, *Complex Intell. Syst.* **2021**, *7*, 1253.

[2] X.-S. Zhang, M.-D. Han, R.-X. Wang, F.-Y. Zhu, Z.-H. Li, W. Wang, H.-X. Zhang, *Nano Lett.* **2013**, *13*, 1168.

[3] J. Kim, A. S. Campbell, B. E.-F. de Ávila, J. Wang, *Nat. Biotechnol.* **2019**, *37*, 389.

[4] Y. Guo, X.-S. Zhang, Y. Wang, W. Gong, Q. Zhang, H. Wang, J. Brugger, *Nano Energy* **2018**, *48*, 152.

[5] F. Wen, Z. Sun, T. He, Q. Shi, M. Zhu, Z. Zhang, L. Li, T. Zhang, C. Lee, *Adv. Sci.* **2020**, *7*, 2000261.

[6] M. Zhu, Z. Sun, Z. Zhang, Q. Shi, T. He, H. Liu, T. Chen, C. Lee, *Sci. Adv.* **2020**, *6*, eaaz8693.

[7] R. Wen, W.-L. Tay, B. P. Nguyen, C.-B. Chng, C.-K. Chui, *Comput. Methods Programs Biomed.* **2014**, *116*, 68.

[8] M. J. Islam, M. Ho, J. Sattar, *J. Field Rob.* **2019**, *36*, 851.

[9] Z. Zhou, K. Chen, X. Li, S. Zhang, Y. Wu, Y. Zhou, K. Meng, C. Sun, Q. He, W. Fan, E. Fan, Z. Lin, X. Tan, W. Deng, J. Yang, J. Chen, *Nat. Electron.* **2020**, *3*, 571.

[10] W. Xu, S. Hu, Y. Zhao, W. Zhai, Y. Chen, G. Zheng, K. Dai, C. Liu, C. Shen, *Nano Energy* **2021**, *90*, 106606.

[11] Y. Liu, H. Khanbareh, M. A. Halim, A. Feeney, X. Zhang, H. Heidari, R. Ghannam, *Nano Select* **2021**, *2*, 1459.

[12] R. Booth, P. Goldsmith, *J. Med. Biol. Eng.* **2018**, *38*, 284.

[13] F. Wen, Z. Zhang, T. He, C. Lee, *Nat. Commun.* **2021**, *12*, 5378.

[14] T. Yang, H. Pan, G. Tian, B. Zhang, D. Xiong, Y. Gao, C. Yan, X. Chu, N. Chen, S. Zhong, L. Zhang, W. Deng, W. Yang, *Nano Energy* **2020**, *72*, 104706.

[15] L. Jin, X. Xiao, W. Deng, A. Nashalian, D. He, V. Raveendran, C. Yan, H. Su, X. Chu, T. Yang, W. Li, W. Yang, J. Chen, *Nano Lett.* **2020**, *20*, 6404.

[16] Y. Si, S. Chen, M. Li, S. Li, Y. Pei, X. Guo, *Adv. Intell. Syst.* **2022**, *4*, 2100046.

[17] M. Wang, Z. Yan, T. Wang, P. Cai, S. Gao, Y. Zeng, C. Wan, H. Wang, L. Pan, J. Yu, S. Pan, K. He, J. Lu, X. Chen, *Nat. Electron.* **2020**, *3*, 563.

**ADVANCED
SCIENCE NEWS**

www.advancedsciencenews.com

**ADVANCED
INTELLIGENT
SYSTEMS**

www.advintellsyst.com

[18] W. Deng, T. Yang, L. Jin, C. Yan, H. Huang, X. Chu, Z. Wang, D. Xiong, G. Tian, Y. Gao, H. Zhang, W. Yang, *Nano Energy* **2019**, *55*, 516.

[19] A. Moin, A. Zhou, A. Rahimi, A. Menon, S. Benatti, G. Alexandrov, S. Tamakloe, J. Ting, N. Yamamoto, Y. Khan, F. Burghardt, L. Benini, A. C. Arias, J. M. Rabaey, *Nat. Electron.* **2021**, *4*, 54.

[20] P. Cai, C. Wan, L. Pan, N. Matsuhisa, K. He, Z. Cui, W. Zhang, C. Li, J. Wang, J. Yu, M. Wang, Y. Jiang, G. Chen, X. Chen, *Nat. Commun.* **2020**, *11*, 2183.

[21] S. Benatti, F. Casamassima, B. Milosevic, E. Farella, P. Schönle, S. Fateh, T. Burger, Q. Huang, L. Benini, *IEEE Trans. Biomed. Circuits Syst.* **2015**, *9*, 620.

[22] X. Liang, H. Li, W. Wang, Y. Liu, R. Ghannam, F. Fioranelli, H. Heidari, *Adv. Intell. Syst.* **2019**, *1*, 1900088.

[23] S. Jiang, B. Lv, W. Guo, C. Zhang, H. Wang, X. Sheng, P. B. Shull, *IEEE Trans. Ind. Inf.* **2018**, *14*, 3376.

[24] P. Tan, X. Han, Y. Zou, X. Qu, J. Xue, T. Li, Y. Wang, R. Luo, X. Cui, Y. Xi, L. Wu, B. Xue, D. Luo, Y. Fan, X. Chen, Z. Li, Z. L. Wang, *Adv. Mater.* **2022**, *34*, 2200793.

[25] G. Li, D. Chen, C. Li, W. Liu, H. Liu, *Adv. Sci.* **2020**, *7*, 2000154.

[26] P. Nie, R. Wang, X. Xu, Y. Cheng, X. Wang, L. Shi, J. Sun, *ACS Appl. Mater. Interfaces* **2017**, *9*, 14911.

[27] H. Chen, Z. Su, Y. Song, X. Cheng, X. Chen, B. Meng, Z. Song, D. Chen, H. Zhang, *Adv. Funct. Mater.* **2017**, *27*, 1604434.

[28] M. Zhu, Y. Yue, Y. Cheng, Y. Zhang, J. Su, F. Long, X. Jiang, Y. Ma, Y. Gao, *Adv. Electron. Mater.* **2020**, *6*, 1901064.

[29] T. Yang, W. Deng, X. Chu, X. Wang, Y. Hu, X. Fan, J. Song, Y. Gao, B. Zhang, G. Tian, D. Xiong, S. Zhong, L. Tang, Y. Hu, W. Yang, *ACS Nano* **2021**, *15*, 11555.

[30] D. Niu, W. Jiang, G. Ye, K. Wang, L. Yin, Y. Shi, B. Chen, F. Luo, H. Liu, *Mater. Res. Bull.* **2018**, *102*, 92.

[31] Y. Wei, S. Chen, X. Dong, Y. Lin, L. Liu, *Carbon* **2017**, *113*, 395.

[32] J. Jia, G. Huang, J. Deng, K. J. N. Pan, *Nanoscale* **2019**, *11*, 4258.

[33] T. Gong, H. Zhang, W. Huang, L. Mao, Y. Ke, M. Gao, B. Yu, *Carbon* **2018**, *140*, 286.

[34] J. Xu, R. Li, S. Ji, B. Zhao, T. Cui, X. Tan, G. Gou, J. Jian, H. Xu, Y. Qiao, Y. Yang, S. Zhang, T.-L. Ren, *ACS Nano* **2021**, *15*, 8907.

[35] J.-N. Ma, J.-W. Mao, D.-D. Han, X.-Y. Fu, Y.-X. Wang, Y.-L. Zhang, *Adv. Mater. Technol.* **2019**, *4*, 1900554.

[36] Y. Hu, H. Ma, W. Liu, Q. Lin, B. Liu, *J. Nanomater.* **2015**, *2015*, 282369.

[37] K. Gurushantha, K. Anantharaju, L. Renuka, S. Sharma, H. Nagaswarupa, S. Prashantha, Y. Vidya, H. Nagabhushana, *RSC Adv.* **2017**, *7*, 12690.

[38] A. C. Ferrari, *Solid State Commun.* **2007**, *143*, 47.

[39] P. B. Shull, S. Jiang, Y. Zhu, X. Zhu, *IEEE Trans. Neural Syst. Rehabil. Eng.* **2019**, *27*, 724.

[40] X. Liang, R. Ghannam, H. Heidari, *IEEE Sens. J.* **2019**, *19*, 1082.

[41] D. Jiang, Y. Wu, A. Demosthenous, *IEEE Trans. Circuits Syst. II Express Briefs* **2020**, *67*, 1554.

[42] N. Siddiqui, R. H. M. Chan, *IEEE Trans. Hum. Mach. Syst.* **2021**, *51*, 56.

[43] Y. T. Liu, Y. A. Zhang, M. Zeng, *IEEE Sens. J.* **2018**, *18*, 10085.